Broadband control of flow of light using plasmonic metasurfaces consisting of arrays of metallic split ring nanoantennas

Seyed M. Sadeghi ■ 0 ; Dustin T. Roberts 0 ; Harrison Knox 0 ; Rithvik R. Gutha 0



J. Appl. Phys. 133, 223104 (2023) https://doi.org/10.1063/5.0155031





Citation

CrossMark

15 December 2023 22:56:12

Crossiviar





Cite as: J. Appl. Phys. 133, 223104 (2023); doi: 10.1063/5.0155031

Submitted: 17 April 2023 · Accepted: 28 May 2023 ·

Published Online: 13 June 2023











Seyed M. Sadeghi, ^{a)} Dustin T. Roberts, DHarrison Knox, Dand Rithvik R. Gutha D





AFFILIATIONS

Department of Physics and Astronomy, University of Alabama in Huntsville, Huntsville, Alabama 35899, USA

a) Author to whom correspondence should be addressed: seyed.sadeghi@uah.edu

ABSTRACT

When a metallic U-shaped nanoantenna (split ring resonator) is observed from its sides, variations in the viewing angle can lead to significantly different size and shape projections. In this study, we demonstrate that plasmonic metasurfaces consisting of arrays of such nanoantennas can support unique side (in-plane) scattering switching and routing processes. These processes encompass a polarization switching \$\vec{\pi}\$ centered at 1.6 µm, which is driven by the coherent excitation of the nanoantennas' multipolar modes. They also include spectrally broad-band (0.5–1.6 µm) directional control of the flow of in-plane light scattering. Such a process includes a total prohibition of light emerging from one side of the metasurface for a given polarization of the incident light. However, when such polarization is rotated by 90, the flow of the in-plane scattering opens with high efficiency. We further discuss the impact of the formation of surface lattice resonance on the coherent amplification of infrared scattering around 1.6 µm and its switching process. The results underscore the influence of variations in asymmetry, 🔉 associated with the sizes and shape projections, on interference processes. They also showcase how in-plane scattering has the capacity to transfer distinct characteristics of plasmonic near-field asymmetries induced by optical fields into far-field scattering.

Published under an exclusive license by AIP Publishing. https://doi.org/10.1063/5.0155031

I. INTRODUCTION

A key application of structural variations of meta-atoms in plasmonic metasurfaces is control of their optical phase distributions and electromagnetic properties. 1-5 Previous reports have shown that this feature can be used to envision broadband anisotropic optical elements, novel waveplates, aberration-free ultrathin flat lenses at telecom frequencies,4 and generation of birefringence. U-shaped nanoantennas or split ring resonators (SRRs) have unique structural forms, making them suitable for harvesting resonant multipolar plasmonic resonances and control of emission properties of quantum emitters. Such nanoantennas have also been studied for applications such as enhancement of second harmonic generation^{7,8} and generation of mid-infrared chirality when combined with graphene gratings. A recent report has also shown that tilted U-shaped nanoantennas can support chirality. 10

The design of meta-atoms' geometric properties enables control over the optical responses of plasmonic metasurfaces, including their far-field scattering. Far-field scattering is a crucial process for extracting information about near-field properties, plasmonic phase, multipolar interference processes, and for envisioning various device applications.² However, when far-field scattering is detected at normal or oblique angles with respect to the metasurfaces' planes, it provides access to only limited classes of multipolar plasmonic phase and interference paths. The situation changes significantly when observing the meta-atoms or plasmonic nanoantennas from their sides, along the planes of their arrays [Fig. 1(a)]. In-plane scattering has previously been utilized to study spin control of quantum dot emissions, polarization control of uniand bidirectional scattering, 11,12 directed emission via multipolar interferences, 13 polarization optical switching via surface lattice resonances,¹⁴ and the formation of plasmonic super-cells associated with arrays of paired V-shaped nanoantennas. 15 The potential of side scattering becomes more evident when considering the impact of symmetry variation associated with the projections of nanoantenna shapes as viewed from the sides [Fig. 1(a)]. In-plane

b)Present address: Ultraleap, Bristol, United Kingdom

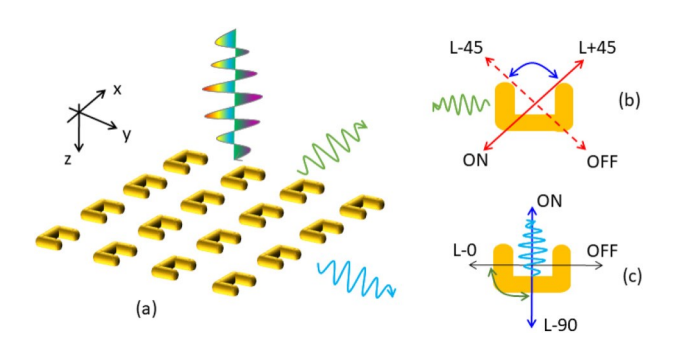


FIG. 1. (a) Schematic of the in-plane polarization switching via arrays of SRRs. (b) and (c) show the states of the spectrally localized optical switching at about 1.6 µm and those of the broadband visible to infrared, respectively.

scattering is expected to be strongly influenced by these side-view projections, resulting in a wide range of plasmonic multipolar phase and coupling categories, as well as position-dependent interference processes.

The objective of this paper is to investigate the impact of symmetry variations associated with the shape and size side-view projections of periodic arrays of Au SRRs on their in-plane scattering in the visible to infrared range (450-1650 nm). As depicted schematically in Fig. 1(a), a linearly polarized broadband light source illuminates the sample at a normal angle. We demonstrate that these arrays can facilitate infrared optical switching at approximately 1.6 µm by enabling enhanced access to the coherent superpositions of multipolar plasmon resonances. This spectrally localized optical switching is unidirectional and is driven by collective modes of the lattice. As illustrated in Fig. 1(b), this process occurs when in-plane scattering is detected along the x-axis, and the incident light polarization alternates between L+45 and L45 (where L+45 and L45 correspond to linear polarization axes at 45 with respect to the x-axis, respectively). Furthermore, our results reveal that when in-plane scattering is

detected along the y-axis [Fig. 1(c)], a broadband optical routing process takes place within the range of 0.5-1.6 µm. This process occurs when the incident light polarization switches between L0 and L+90 (where L0 and L+90 represent linear polarization along the xaxis and y-axis, respectively). For L0, no light flows along the y-axis of the array, resulting in an OFF (dark) state. However, when polarization switches to L+90, the flow of light from this side becomes highly efficient. These findings emphasize the complete suppression of scattering through interference processes between various multipolar modes and the ability of in-plane scattering to transfer near-field asymmetries induced by optical fields into farfield scattering.

II. METHODS AND EXPERIMENTATION

Samples consisting of arrays of Au SRRs were fabricated using E-beam lithography on glass substrates. Figure 2(a) shows the topview of a scanning electron microscopy (SEM) image of such samples. The lattice constant along the x-axis (a_x) and the y-axis (a_v) of arrays were 1.5 and 1 μm, respectively. The two arms of the SRRs had length (L₁) of about 330 nm [Fig. 2(b)], their lengths along the x-axis (L) were 990 nm, and their heights were about 40 nm. The extinction spectra of such a structure when the incident light reaches the samples at normal angle with polarization along the x-axis (x-pol) and y-axis (y-pol) are shown in Fig. 2(c). The results show that for x-pol (solid line), the spectrum supports two peaks, one at about 822 nm (peak A) and the other at 1180 (peak B). For y-pol (dashed lines), the arrays support a peak at about 790 nm = (peak C) and another one at about 1425 nm (peak D).

To analyze the impact of phase and multipolar modes dictated by viewing the sample from the side, we spectrally and locally analyze the in-plane scattering of the arrays. For this, we used an & optical setup consisting of a broad white light source passing a 8 linear polarizer and then a microscope objective (objective 1) to focus the light on the samples with a given polarization [Fig. 2(d)]. The scattered light was then collected by a second microscope objective (objective 2). As schematically shown in Fig. 2(d),

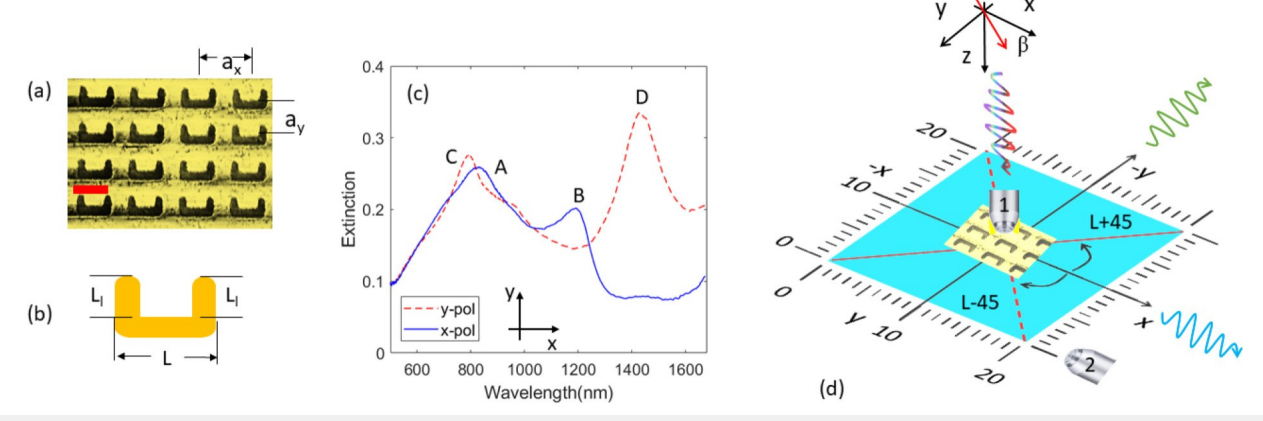


FIG. 2. (a) Top view SEM images of the SRR array. (b) Schematics of the lateral sizes of a single SRR. (c) Extinction spectra of array for x-pol (solid lines) and y-pol (dashed lines). (d) Schematic of in-plane scattering configuration. The red scale bar in (a) is $1 \mu m$.

resilient (squares). In contrast to the cases presented in Figs. 3(a) and 3(b), when the axis of rotation is along the x-axis, for x-pol, we mostly see amplitude suppression for peaks A and B, without major wavelength shift [Fig. 3(c)]. For y-pol, however, one can see a clear doubling of peak C and red shift of peak D accompanied with strong amplitude suppression.

The results associated with peak C can be analyzed by considering the fact that when the incident light reaches the sample at a normal angle, the resonant modes of the lattice (Rayleigh anomaly modes) degenerate. However, at oblique angles, these degeneracies

the rotation remains unchanged but the incident light becomes

polarized along the y-axis (y-pol), peaks C and D are mostly red

shifted. In the case of peak D, however, the amplitude remains

objective 2 was moved along the edges of the substrates of the arrays, mapping the in-plane scattering at different positions. The range of movement of this objective was between 0 and 20 mm, i.e., the whole length of the sides of the glass substrates supporting the arrays. The angle of polarization of incident light (β) was measured with respect to the x-axis [Fig. 2(d)]. To analyze the plasmonic modes of the SRR array, we analyze their mode properties using finite difference time domain (FDTD) simulation method. For this, we used the Device Multiphysics Simulation Suite of Lumerical software (2020a version).

The results associated with peak C can be analyzed by considering the fact that when the incident light reaches the sample at a normal angle, the resonant modes of the lattice (Rayleigh anomaly modes) degenerate. However, at oblique angles, these degeneracies are lifted, resulting in a spectral gap that increases with the incident angle. ^{18–20} These modes can be investigated by analyzing the changes in the extinction spectra as the samples are rotated. Specifically, at around 800 nm, as illustrated in Fig. 3(d), distinct diffractive modes are observed, characterized by the appearance of peaks centered at this wavelength (squares and circles). To analyze this further, the variations of the wavelengths of the Rayleigh Anomaly (RA) modes with the incident angle can be expressed as follows:

III. MODE CHARACTERIZATION

$$\lambda_{RA} \% \frac{a}{m} [n + \sin(\theta_r)]$$
: (1)

The optical features seen in Fig. 2(c) can be associated with the multipolar plasmonic modes of SRRs and the impact of their arrays, including formation of surface lattice resonances (SLRs). $^{16-18}$ To characterize these features, we studied the extinction spectra of the SRR arrays when they were rotated along the x- and y-axes. Under these conditions, the angle between the normal to the surface of the array and the incident light (θ_r) was changed. Figure 3(a) shows the results when the sample was rotated along the y-axis, and the incident light was polarized along the x-axis (x-pol). Here, curves highlighted with lines 1–5 refer to the extinction spectra of the arrays for θ_r ¼ 0, 10, 15, 20, and 25, respectively. These results show that peak A seems to become broadened with some indications of splitting. On the other hand, peak B undergoes blue shift with strong amplitude suppression. In fact, when θ_r ¼ 15 (line 3), this peak disappears. When the axis of

Here, a refers to the lattice constant of the array $(a_x \text{ or } a_y)$, θ_r is the incident angle, n is the refractive index $(n_{sub}$ for the substrate, and n_{sup} is the superstrate), and m to the order of the diffraction. Judging

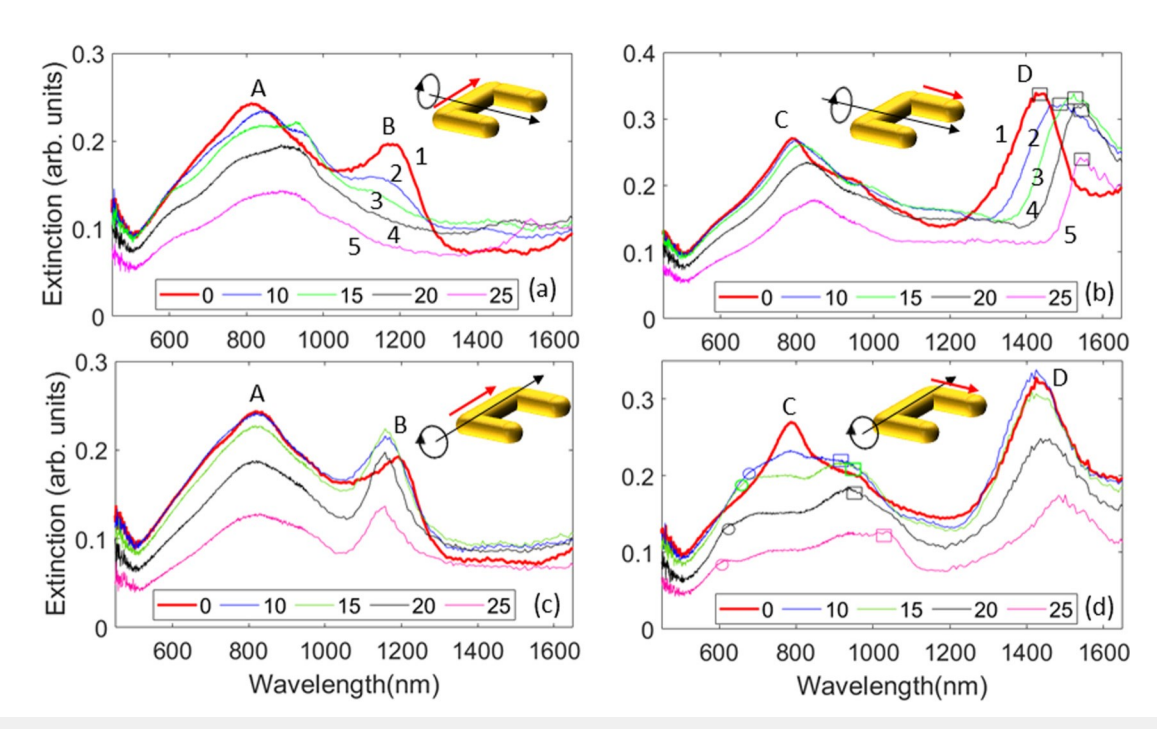


FIG. 3. Evolution of the extinction spectra of SRR arrays when the axis of rotation is y-axis [(a) and (b)] and x-axis [(c) and (d)]. In (a) and (c), the incident light is polar-ized along x-axis and in (b) and (d), along the y-axis. The plots highlighted with numbers 1–5 represent the extinction spectra for θ_r ½ 0, 10, 15, 20, and 25, respectively.

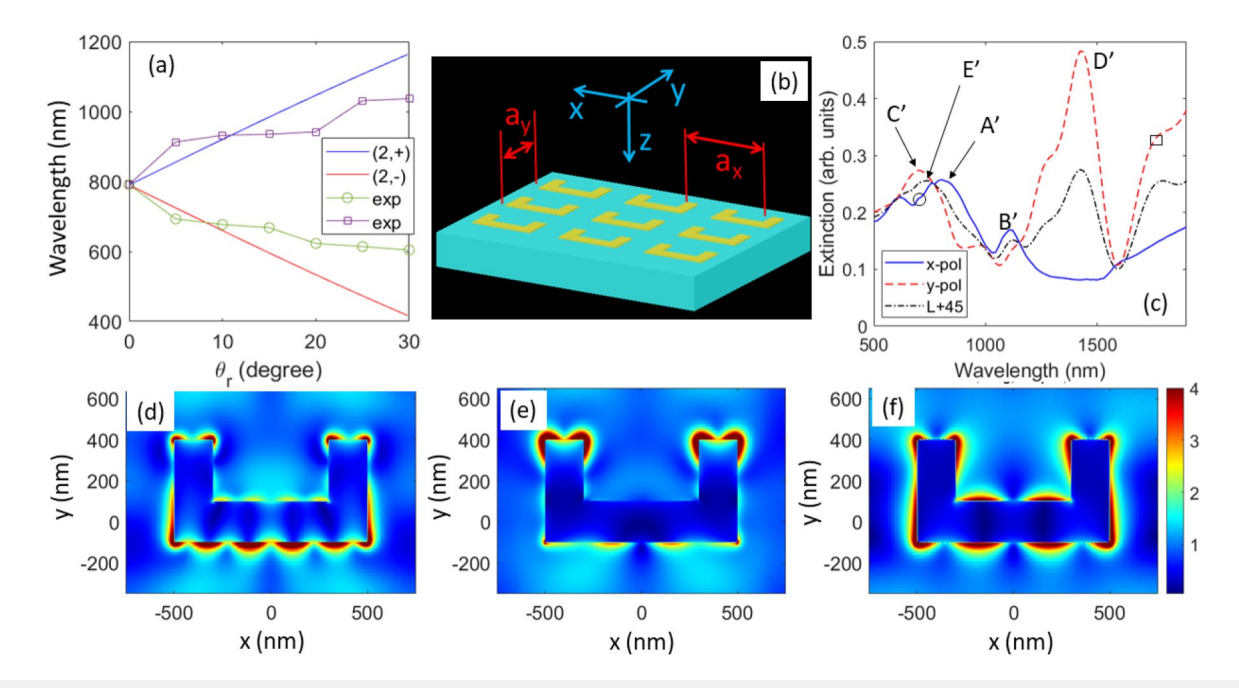


FIG. 4. (a) Results of calculation of RA wavelengths. (b) Schematic of the system structure used for simulation of the extinction spectra of the SRR array. (c) Simulation results for the extinction spectra for x-pol (solid line), y-pol (dashed line), and L+45 (dashed-dotted line). (d)–(f) Modal field enhancement factors in the x–y plane at 727 (circle), 787 (peak A⁰), 1106 nm (peak B⁰), respectively, when the incident beam is polarized along x-axis. The vertical color-coded bar refers to the range of the field enhancement factor.

by the values of a_x ½ 1:5 and a_y ½ 1 µm, we can associate the splitting seen in Fig. 3(d) (peak C) with SLR having second order diffraction m ½ 2. The results of calculations of variations λ_{RA} as a function of θ_r are shown in Fig. 4(a). Here, the solid and dashed lines refer to λ_{RA} for (2,+) and (2,) modes. The circles and squares correspond to the wavelengths highlighted with circles and squares in Fig. 3(d). To obtain λ_{RA} , we assumed n_{sup} =1, i.e., diffraction occurs in air (superstrate).

To further explore the mode properties of the SRR arrays and the impact of the lattice coupling, we numerically studied the near field mode profiles of arrays for the resonances seen in the extinction spectra. This was done considering a SRR with similar dimensions as in the samples and with periodic boundary conditions along the x- and y-axes. The substrate was modeled as glass, and the superstrate was air, reflecting the experimental conditions. The incident light was assumed to illuminate the structure from the top [Fig. 4(b)]. The incident light reached this structure from the top [Fig. 4(b)]. Figure 4(c) shows the results of simulation for the extinction spectra for x-pol (solid line), y-pol (dashed line), and L +45 (dashed-dotted line). The L45 spectrum was found to be identical to that of the L+45. Comparing with the experimental results shown in Fig. 2(c), the results in Fig. 4(c) for x-pol and y-pol show the main features, although lack of inclusion of edge roundness, shapes and size fluctuations have led to some discrepancies. Figures 4(d)-4(f) show the modal field enhancement factors, defined as the field intensity in the presence of the nanoantennas arrays to that in their absence, for x-pol at different wavelengths. These results suggest distinct longitudinal multipolar plasmonic

modes at 727 nm [Fig. 4(c), circle]. At the peak at about 787 nm [Fig. 4(c), circle]. At the peak at about 787 nm [Fig. 4(c)], this feature is replaced with transverse modes of the arms of the SRRs [Fig. 4(c)]. At 1106 nm (peak B⁰), both the transverse and longitudinal plasmonic modes of the arms and bases of the nanoantennas are excited [Fig. 4(f)].

For y-pol, as shown in Fig. 4(c) (dashed line), the simulation results suggest two major peaks at 712 (peak C⁰) and 1424 nm (peak D⁰). At 1787 nm also we see an optical feature (square), which is beyond the range of our spectroscopy system. Peak Do is of particular interest since it is associated with peak D in Fig. 2(c). Figure 5 shows the modal field enhancement at 666 (a), 1272 (b), 1474 (c), and 1787 nm (d) in the x-y plane for y-pol. Similar to the case of Figs. 4(d)-4(f), this plane passes through the middle of the nanoantenna heights, i.e., 20 nm from the substrate. The modes at 1424 and 1787 nm are of particular interest here. The results in the case of 1424 (peak D0) suggest mode bending at the corners and middle of the base of the SRRs [Fig. 5(c)]. Figures 5(e) and 5(e⁰) show the modal enhancement factors at this wavelength in the x-z and y-z planes, respectively. These planes are perpendicular to the x-y plane, crossing it along the x- and y-axes, as indicated with arrows in Fig. 5(c). The results show that along the x-axis, the modes are coupled optically via superstrate [Fig. 5(e)]. Optical coupling between the nanoantennas also occurs along the y-axis [Fig. 5(e⁰)]. This suggests that peak D⁰ is associated with optical coupling of the SRR modes. Around the wavelength of the feature seen at 1787 (square), the situation is rather different. As seen in Fig. 5(d), for this case, in the x-y plane, the field is more concentrated inside the SRRs and modes at the edges are weaker.

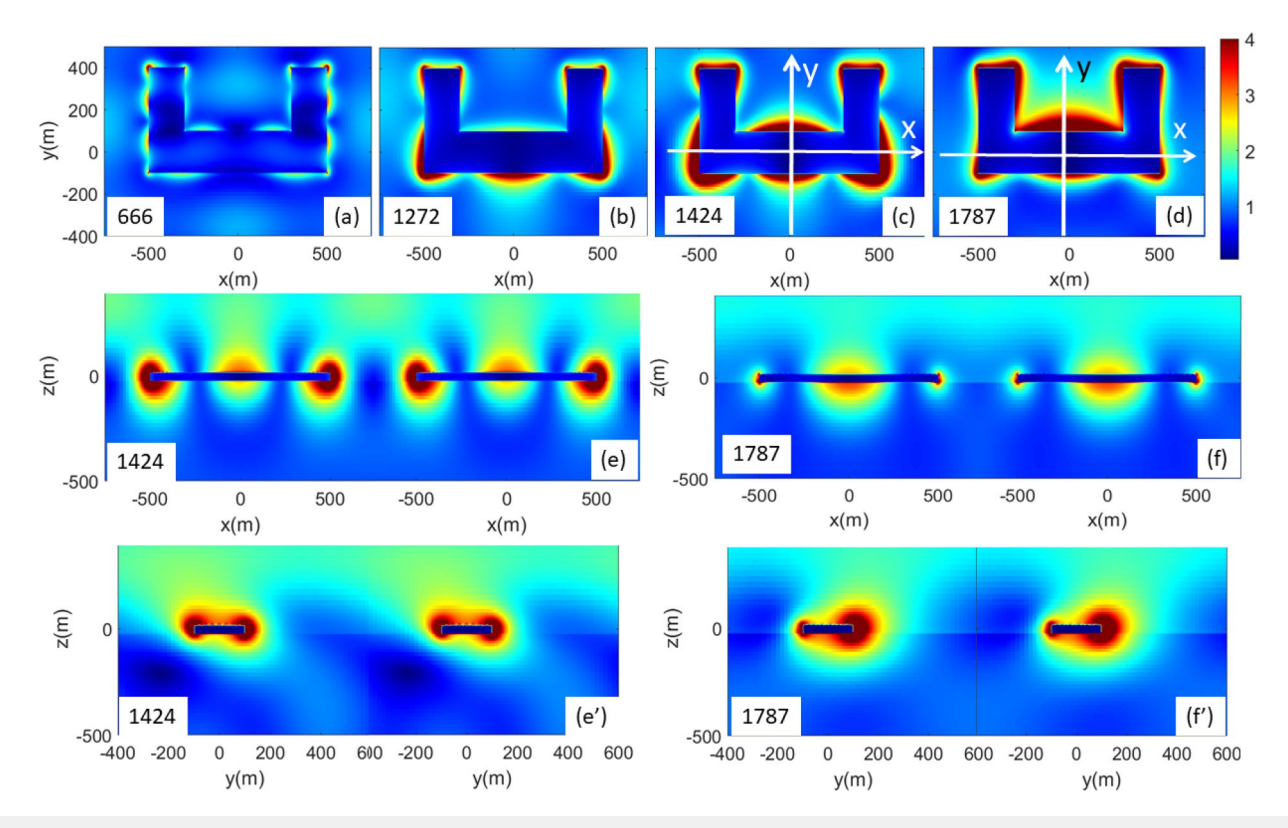


FIG. 5. Modal field enhancement factors in the x-y plane for y-pol at 666 (a), 1272 (b), 1472 (c) and 1787 nm. (e) and (f) show the field enhancement factors in the x-z plane at 1424 and 1787 nm, respectively. (e⁰) and (f⁰) show the field enhancement factors in the y-z plane at 1424 and 1787 nm, respectively. In (a)–(d), one unit cell is shown, but in (e)–(f⁰), two unit cells are considered. The vertical color-coded bar refers to the range of the field enhancement factor. The arrows in (c) and (d) refer to the intersections of x-z [(e) and (f)] and y-z planes [(e⁰) and (f⁰)] with the x-y plane.

Additionally, along the x-axis (x-z plane) and y-axis (y-z plane), as seen in Fig. $5(f^0)$ and $5(f^0)$, mostly the transverse modes associated with the base penetrate deeply into the superstrate, indicating lesser level of collective excitation.

The results shown in Fig. 4 indicate that for x-pol, beyond 1100 nm, i.e., peak B⁰, no major mode occurs. For the case of y-pol, however, as seen in Fig. 5, the two major modes happen in the infrared range, one at 1424 (peak D⁰) and 1787 nm (square). As expected for both cases, however, the plasmonic modes were symmetric along the y-axis. The situation changes significantly when the incident light has L+45 and L45 polarization. To see this, we carried our simulation under the same conditions as those in Figs. 4 and 5 but the cases when β ¼ 45 and 45 [Fig. 2(c)]. Figure 4(c) (dashed line) shows the results for the extinction spec-trum of L+45, which were found to be identical to that of L45. The near field inspection of L+45 and L45, however, offers two different perspectives. To see this, in Fig. 6, we show the modal field enhancement at four wavelengths (numbers in legends in nm). Here, (a)-(d) refer to the case of L45 and (a⁰)-(d⁰) to that of L+45. The results suggest that although the extinction spectra of L+45 and L45 are found to be identical, there are some distinct amounts of asymmetries in their near fields. For the cases of 747 [peaks E⁰ in Fig. 4(c)] and 1151 nm (peak B⁰), the results suggest a

flipping of the modes from L45 to L+45. Mode flipping can be also seen at 1424 and 1787 nm. In the case of 1787 nm, however, it is more pronounced as field accumulation inside of the U-shaped nanoantennas on the left or right side [Figs. 6(d) and 6(d⁰)]. Similar to the case of linear polarization, such asymmetry do not generate any feature in the far field. In Sec. IV, it is shown that such asymmetries can, however, be carried by far field in-plane scattering.

IV. INFRARED UNIDIRECTIONAL IN-PLANE OPTICAL SWITCHING

To investigate how in-plane scattering can provide information regarding the near field asymmetry generated by the incident light polarization, we follow the optical setting highlighted in Fig. 2(c). For this, objective 2 scanned the whole four sides of the glass substrate supporting the arrays. The results for in-plane scattering detected along the x-axis within the range of 520–1650 nm are shown in Fig. 7. Here, (a)–(d) refer to the cases when the incident light was considered to be polarized along β ¼ 45 (L45), 0 (L0), 45 (L+45), and 90 (L90), respectively. These results suggest significant differences in the in-plane scattering intensity and spectrum as the incident light polarization varies. They show

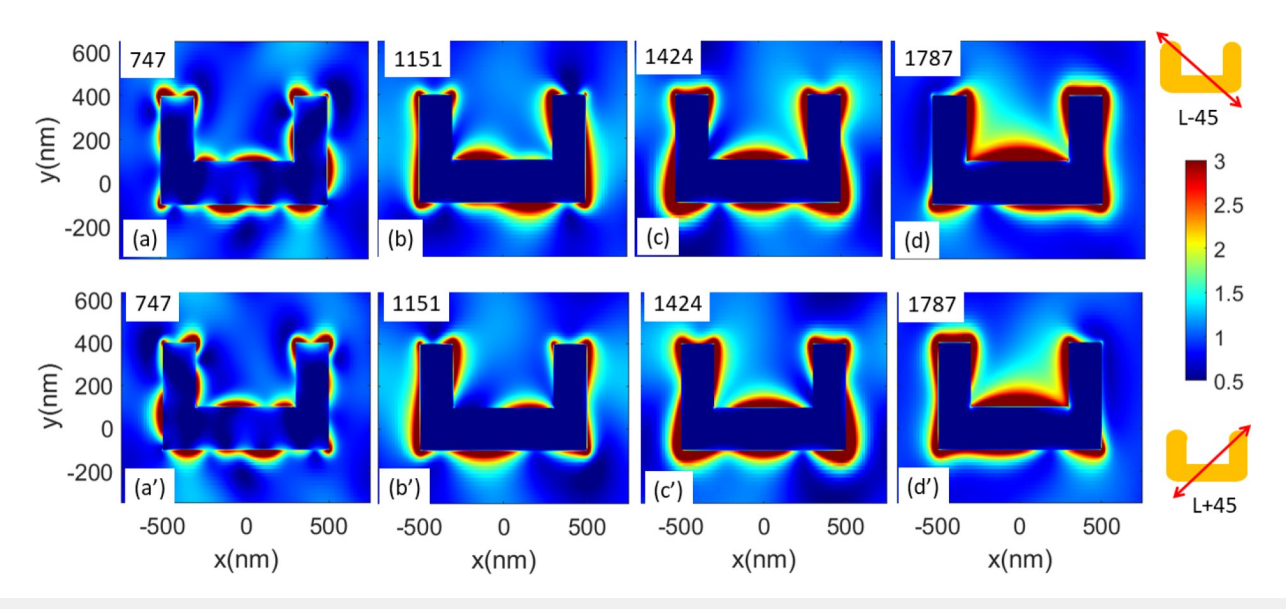


FIG. 6. Modal field enhancement factors in the x-y plane for the case of L45 [(a)-(d)] and L+45 $[(a^0)-(d^0)]$. The numbers on the left-top sides in each panel refer to the wavelength in nm.

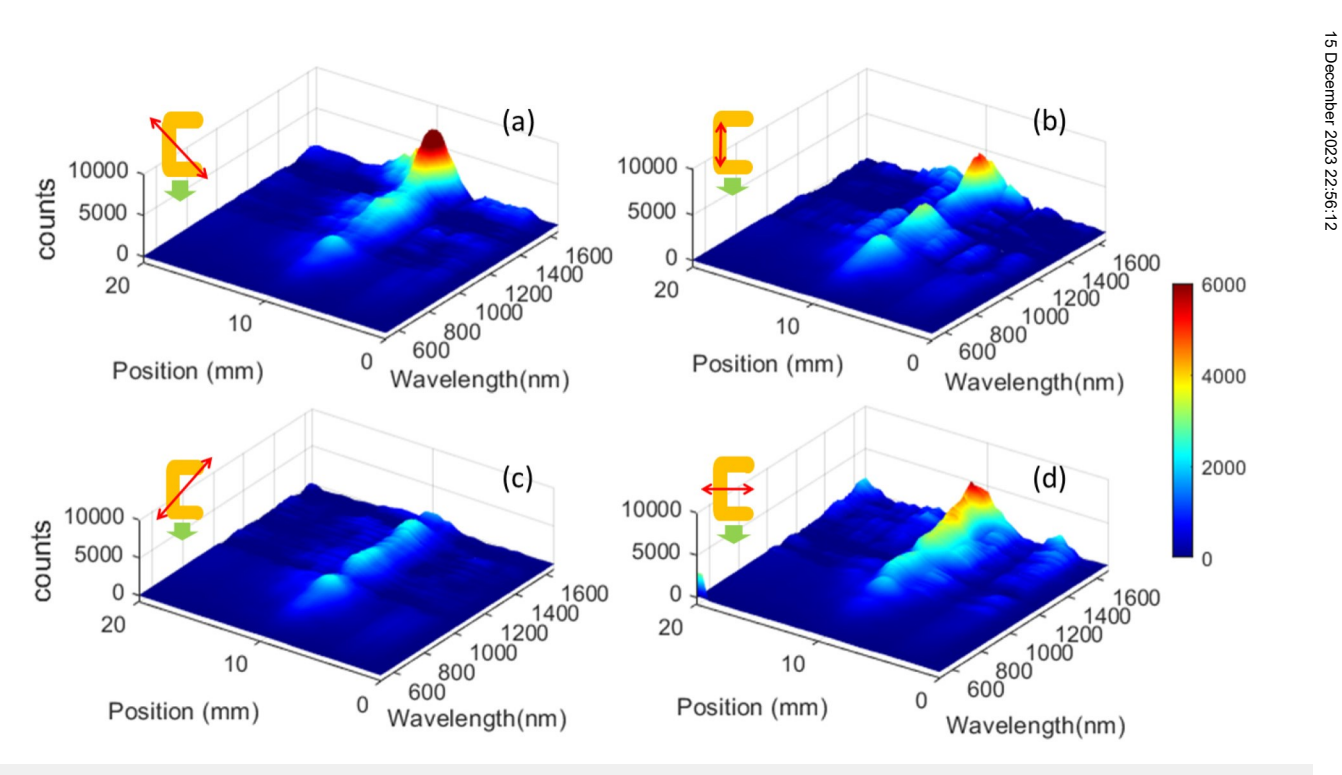


FIG. 7. The in-plane scattering of SRRs arrays as a function of positions when it is measured along x-axis and the incident light polarization is L45 (a), L0 (b), L+45 (c), or L90 (d). The inset in each figure shows the direction of scattering detection (green arrows) and the axis of polarization of the incident light (double-sided red arrows). The numbers on the scale bars refer to the detection counts.

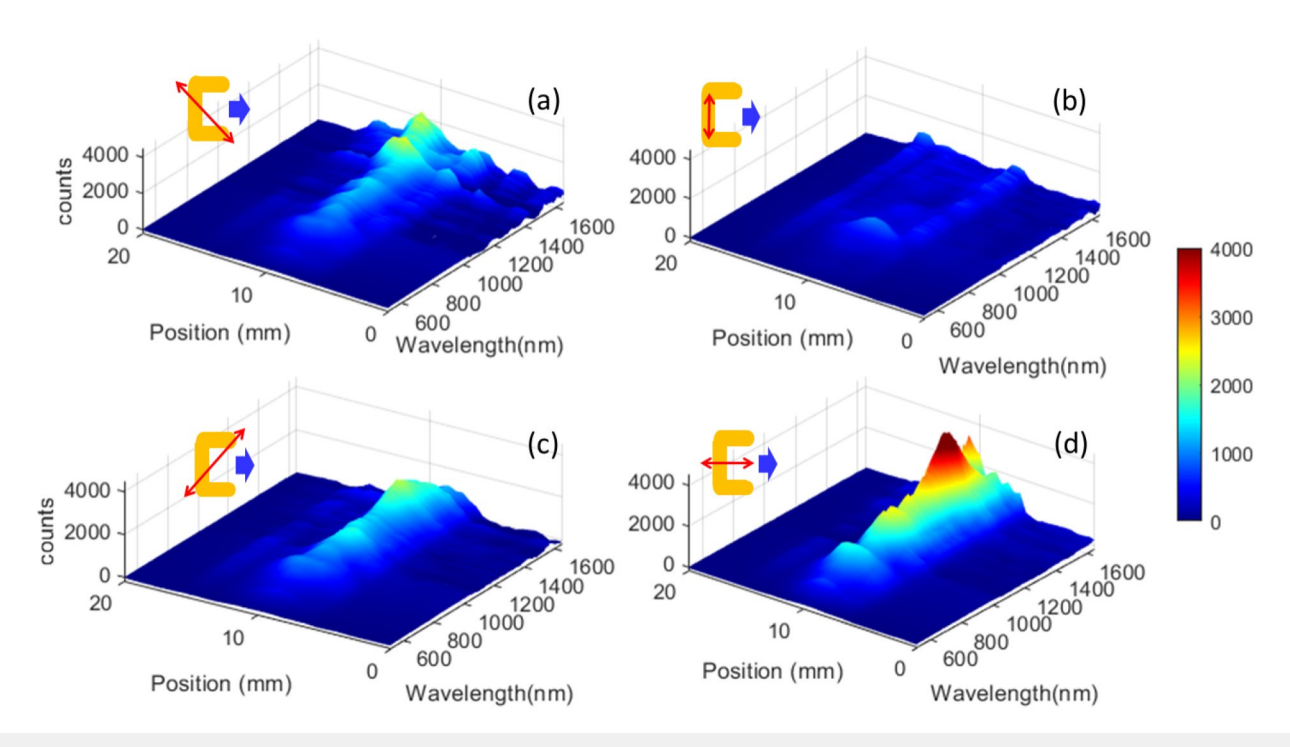


FIG. 8. Similar to Fig. 7 but when the scattering is detected along the y-axis.

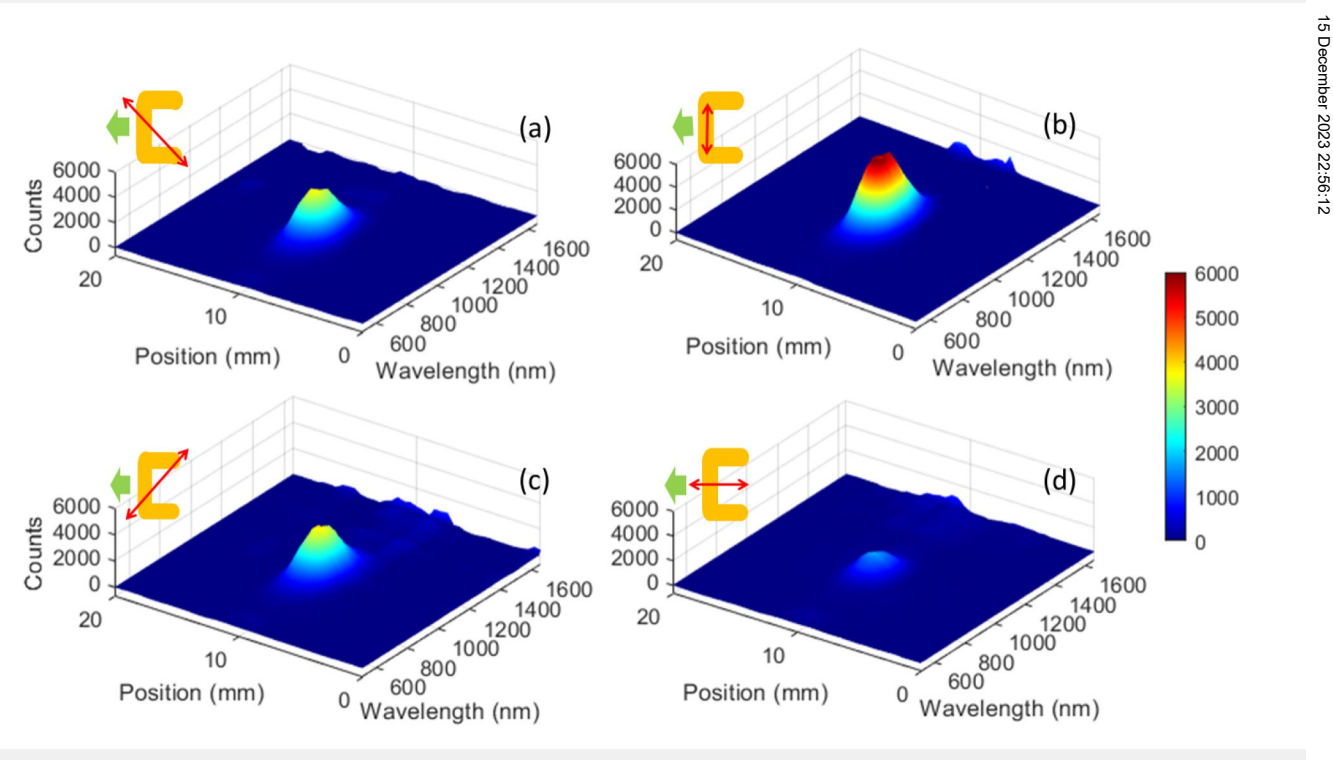


FIG. 9. The in-plane scattering of SRRs arrays as a function of positions when it is measured along the y-axis and the incident light polarization is L45 (a), L0 (b), L+45 (c), or L90 (d). The inset in each figure shows the direction of light detection (green arrows) and axis of polarization of the incident light (double-sided red arrows). The numbers on the scale bar refer to the detection counts.

how variations of the side-view projections of the shapes and sizes of the SRRs and, therefore, nanoantennas asymmetries influence the phase and multipolar plasmonic contributions to the scatter-ing. A key observation here belongs to the case of L45, where we can see a strong scattering peak at about 1610 nm [Fig. 7(a)]. Switching of this polarization to L45 dramatically suppresses this peak by about one order of magnitude [Fig. 7(c)]. This suggests an infrared directional switching process for 1610 nm. More specifi-cally, such a process allows spectral extraction of the broad inci-dent white light into a certain side of the arrays within a relatively narrow wavelength range.

The results shown in Figs. 7(a) and 7(c) can be related to the mode profiles shown in Figs. 6(d) and 6(d⁰). Therefore, they are indication of the near field asymmetries induced by the L+45 and L45, causing either near complete destruction of the far field scattering [Fig. 7(c)] or its efficient flow centered at 1610 nm. Such phenomena can be related to interference processes along the direction of observation of the far field scattering, i.e., the x-axis. ^{13,21,22} The results for the case when the in-plane scattering was detected along the y-axis can also provide unique features. Here, the main outcomes can be inferred from comparison of results for the case of L0 [Fig. 8(b)] and L+90 [Fig. 8(d)]. These results suggest that

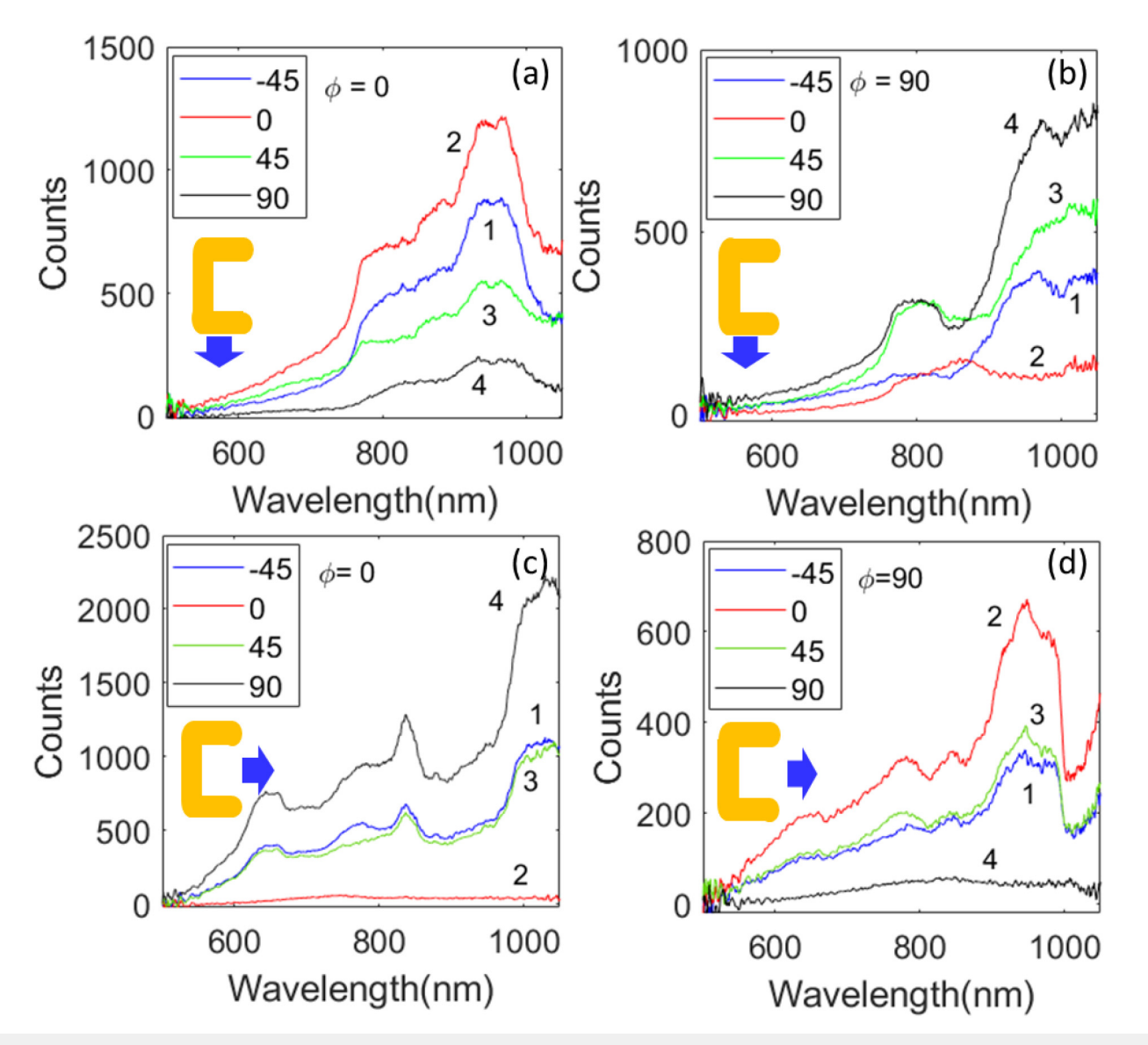


FIG. 10. In-plane scattering detected along the x-axis [(a) and (b)] and along the y-axis [(c) and (d)] for L45 (line 1), L0 (line 2), L+45 (line 3), and L90 (line 4). In (a) and (c), f ¼ 0 and in (b) and (d), f ¼ 90.

when the SRRs are viewed toward their troughs (y-axis), a wideband routing process can happen. In fact for the case of L0, nearly no light is detected emerging along the y-axis [Fig. 8(b)]. When the incident light polarization switches to L+90, however, scattering occurs efficiently within the 500-1650 nm range with a peak at about 1500 nm. This nearly covers the whole spectral range of the incident white light.

The results in Fig. 8 highlight, again, possible unique interference processes happening when the in-plane scattered light is detected along the y-axis. In the case of Fig. 8(b) a clear destructive effect in the scattering associated with the multipolar plasmons can be seen. The contrast between the modes for x-pol (L0) and y-pol (L+90) are shown in Figs. 4(d)-4(f) and Figs. 5(a)-5(d), respectively. In the case of L0, no significant mode can be beyond 1100 nm. In the case of L+90, however, pronounced modes can be seen over the detected spectral range, i.e., 500-1650 nm [Figs. 5(a)-5(d)]. This situation undergoes dramatic changes, if the scattering is detected along the y-axis. As shown in Fig. 9, when the shape projections do not contain a significant proportion of the arms of SRRs, the scattering solely concentrated in around 1000 nm. Under this condition, polarization optical switching can be seen for the cases of L0 and L+90 [Figs. 9(b) and 9(d)]. This is rather in contrast to what is seen in Figs. 8(b) and 8(d), wherein for L0, no scattering occurs, while for L+90, it becomes efficient.

V. POLARIZATION CONVERSION VIA SPLIT RING RESONATOR ARRAYS

The symmetric SRRs studied in this paper can be brought into congruence with a mirror image. A recent report, however, suggested that if the plasmonic multipolar moments of such a structure is driven by a quantum dot, the spin of the QD emission the system can be controlled, generating circularly polarized fluorescence. The key premise of such a process is the resonant excitation of at least two multipolar moments, causing electric fields with appropriate phase, directions, and proportions. The scattering patterns of the SRR arrays studied in this paper, however, can be related to the multipolar contributions with phase properties dictated by the size and phase projections of the nanoantennas.

To study these features further, we analyze the polarization of the in-plane scattering of this array. For this, we put a polarization analyzer at the back of the objective 2 [Fig. 2(c)], before delivering the light to the spectrometers. The results are presented in Fig. 10. Here, f ¼ 0 refers to the case when the axis of the analyzer was perpendicular to the plane of the array and f 1/4 90 to the case when it was parallel to this plane. The results shown in Fig. 10(a) indicate that, when the in-plane scattered was detected along the x-axis and f ¼ 0, for all incident light polarization (β), the in-plane scattering spectra have more or less similar spectra with a peak at about 900 nm (legends show the values of β). These spectra also have smaller peaks at about 800 nm. When the analyzer axis is rotated by 90, i.e., f ¼ 90, as shown in Fig. 10(b), the peak around 800 nm becomes more distinct, but the majority of scattering power is now concentrated at about 1000 nm and longer. In both cases of f ¼ 0 [Fig. 10(a)] and f ¼ 90 [Fig. 10(b)], one can see the spectra of scattered light for L90 and L+90 are different. This can be an indication of elliptical polarization.

Under the same conditions, the polarization states of the in-plane light scattering along the y-axis seem different. Figure 10(c) show the vertical component of scattered light component (f ¼ 0) for different incident light polarization (β), indicating three main wavelengths, i.e., 650, 840, and 1025 nm, with distinct features. Here, however, the spectra associated with β ¼ 45 (L+45) and 45 (L45) overlap. Also, judging by the fact, the intensity of scattered light for β ¼ 0 (L0) becomes very small, one can infer this offers a nearly polarized light. The case of f ¼ 90 [Fig. 9(d)] also offers a nearly polarized case. Here, however, scattered light is more concentrated around 950 nm.

VI. CONCLUSIONS

We studied application of interference processes associated with multipolar plasmon resonances in arrays of SRRs for control and routing of far field scattering in the visible to infrared range. The main premise of this was to detect the side scattering, rather than front or back scattering, to demonstrate the profound impact of size and shape projections of SRRs on the interference processes in the far field scattering of the arrays. We demonstrated complete suppression of scattering from one side of the arrays for a given polarization of the incident light. By changing the state of such polarization, the flow of scattered light occurs in a broad range of wavelengths from 600 to 1650 nm. Our results also showed that the mutlipolar plasmon moments associated with the SRRs can have an augmented impact on the in-plane scattering, allowing extraction of incident light spectral content into a narrow optical range (1.6 µm) from one side of the array. Such outcomes promote in-plane scattering as a unique carrier for transfer of local asymmetric nanoantennas near fields into far fields.

ACKNOWLEDGMENTS

This research was supported by U.S. National Science tion of incident light spectral content into a narrow optical range

Foundation under Grant No. ECCS-1917544.

AUTHOR DECLARATIONS

Conflict of Interest

The authors have no conflicts to disclose.

Author Contributions

Seyed M. Sadeghi: Conceptualization (lead); Formal analysis (lead); Funding acquisition (lead); Project administration (equal); Supervision (equal). Dustin T. Roberts: Data curation (equal); Methodology (equal). Harrison Knox: Data curation (equal). Rithvik R. Gutha: Data curation (equal).

DATA AVAILABILITY

The data that support the findings of this study are available within the article.

REFERENCES

¹M. A. Kats, P. Genevet, G. Aoust, N. Yu, R. Blanchard, F. Aieta, Z. Gaburro, and F. Capasso, "Giant birefringence in optical antenna arrays with widely tailorable optical anisotropy," Proc. Natl. Acad. Sci. U.S.A. 109, 12364-12368 (2012).

- ²H.-T. Chen, A. J. Taylor, and N. Yu, "A review of metasurfaces: Physics and applications," Rep. Prog. Phys. **79**, 076401 (2016).
- ³N. Yu, F. Aieta, P. Genevet, M. A. Kats, Z. Gaburro, and F. Capasso, "A broadband, background-free quarter-wave plate based on plasmonic metasurfaces," Nano Lett. 12, 6328–6333 (2012).
- ⁴F. Aieta, P. Genevet, M. A. Kats, N. Yu, R. Blanchard, Z. Gaburro, and F. Capasso, "Aberration-free ultrathin flat lenses and axicons at telecom wavelengths based on plasmonic metasurfaces," Nano Lett. 12, 4932–4936 (2012).
- ⁵J. Sung, M. Sukharev, E. M. Hicks, R. P. Van Duyne, T. Seideman, and K. G. Spears, "Nanoparticle spectroscopy: Birefringence in two-dimensional arrays of L-shaped silver nanoparticles," J. Phys. Chem. C 112, 3252–3260 (2008).
 ⁶S. S. Kruk, M. Decker, I. Staude, S. Schlecht, M. Greppmair, D. N. Neshev, and Y. S. Kivshar, "Spin-polarized photon emission by resonant multipolar nanoantennas," ACS Photonics 1, 1218–1223 (2014).
- ⁷S. Keren-Zur, O. Avayu, L. Michaeli, and T. Ellenbogen, "Nonlinear beam shaping with plasmonic metasurfaces," ACS Photonics 3, 117–123 (2016).
- ⁸L. Michaeli, S. Keren-Zur, O. Avayu, H. Suchowski, and T. Ellenbogen, "Nonlinear surface lattice resonance in plasmonic nanoparticle arrays," Phys. Rev. Lett. 118, 243904 (2017).
- ⁹Z. Huang, K. Yao, G. Su, W. Ma, L. Li, Y. Liu, P. Zhan, and Z. Wang, "Graphene–metal hybrid metamaterials for strong and tunable circular dichroism generation," Opt. Lett. 43, 2636–2639 (2018).
- ¹⁰T.-K. Wang, T. Fu, Y. Chen, and Z. Zhang, "Circular dichroism of a tilted U-shaped nanostructure," Opt. Lett. 42, 2842–2845 (2017).
- ¹¹D. Vercruysse, X. Zheng, Y. Sonnefraud, N. Verellen, G. D. Martino, L. Lagae, G. A. E. Vandenbosch, V. V. Moshchalkov, S. A. Maier, and P. Van Dorpe, "Directional fluorescence emission by individual V-antennas explained by mode expansion," ACS Nano 8, 8232–8241 (2014).
- ¹²D. Vercruysse, Y. Sonnefraud, N. Verellen, F. B. Fuchs, G. D. Martino, L. Lagae, V. V. Moshchalkov, S. A. Maier, and P. Van Dorpe, "Unidirectional

- side scattering of light by a single-element nanoantenna," Nano Lett. 13, 3843–3849 (2013).
- ¹³I. M. Hancu, A. G. Curto, M. Castro-López, M. Kuttge, and N. F. van Hulst, "Multipolar interference for directed light emission," Nano Lett. 14, 166–171 (2014).
- ¹⁴S. M. Sadeghi, R. R. Gutha, S. Ramsay, D. Roberts, and C. Sharp, "Polarization optical switching based on the molding of coherent light scattering via surface lattice resonances," Mater. Today Nano 18, 100190 (2022).
- ¹⁵S. M. Sadeghi, D. T. Roberts, R. R. Gutha, S. Allen, and C. Sharp, "Polarization optical switching between supercell states of plasmonic metasurfaces," Phys. Rev. A 106, 063518 (2022).
- ¹⁶S. M. Sadeghi, W. J. Wing, and Q. Campbell, "Tunable plasmonic-lattice mode sensors with ultrahigh sensitivities and figure-of-merits," J. Appl. Phys. 119, 244503 (2016).
- ¹⁷V. G. Kravets, A. V. Kabashin, W. L. Barnes, and A. N. Grigorenko, "Plasmonic surface lattice resonances: A review of properties and applications," Chem. Rev. 118, 5912–5951 (2018).
- ¹⁸S. R. K Rodriguez, M. C. Schaafsma, A. Berrier, and J. Gómez Rivas, "Collective resonances in plasmonic crystals: Size matters," Physica B 407, 4081–4085 (2012).
- ¹⁹S. R. K Rodriguez and J. Gómez Rivas, "Surface lattice resonances strongly coupled to rhodamine 6G excitons: Tuning the plasmon-exciton-polariton mass and composition," Opt. Express 21, 27411–27421 (2013).
- ²⁰S. M. Sadeghi, R. R. Gutha, and W. J. Wing, "Turning on plasmonic lattice modes in metallic nanoantenna arrays via silicon thin films," Opt. Lett. 41, 3367–3370 (2016).
- ²¹J. Lin, J. P. Balthasar Mueller, Q. Wang, G. Yuan, N. Antoniou, X.-C. Yuan, and F. Capasso, "Polarization-controlled tunable directional coupling of surface plasmon polaritons," Science 340, 331–334 (2013).
- ²²J. González-Colsa, G. Serrera, J. M. Saiz, F. González, F. Moreno, and P. Albella, "On the performance of a tunable grating-based high sensitivity unidirectional plasmonic sensor," Opt. Express 29, 13733–13745 (2021).